Open Veterinary Journal, (2024), Vol. 14(3): 885-894
ISSN: 2226-4485 (Print)
ISSN: 2218-6050 (Online)

Original Research
DOI: *10.5455/OVJ.2024.v14.i3.16*

Submitted: 24/01/2024 Accepted: 29/02/2024 Published: 31/03/2024

Finite element study on post-screw removal stress in toy poodle radius with different plate designs and screw arrangements

Dito Anggoro[1,2], Melpa Susanti Purba[1], Fei Jiang[3], Norihiro Nishida[4], Harumichi Itoh[5], Kazuhito Itamoto[5], Yuki Nemoto[6], Munekazu Nakaichi[6], Hiroshi Sunahara[7] and Kenji Tani[7*]

[1]*Laboratory of Veterinary Surgery, Joint Graduate School of Veterinary Medicine, Yamaguchi University, Japan*
[2]*Department of Surgery and Radiology, Faculty of Veterinary Medicine, Gadjah Mada University, Indonesia*
[3]*Department of Mechanical Engineering, Graduate School of Sciences and Technology for Innovation, Yamaguchi University, Japan*
[4]*Department of Orthopedic Surgery, Graduate School of Medicine, Yamaguchi University, Japan*
[5]*Laboratory of Small Animal Clinical Science, Joint Faculty of Veterinary Medicine, Yamaguchi University, Japan*
[6]*Laboratory of Veterinary Radiology, Joint Faculty of Veterinary Medicine, Yamaguchi University, Japan*
[7]*Laboratory of Veterinary Surgery, Joint Faculty of Veterinary Medicine, Yamaguchi University, Japan*

Abstract

Background: The study employs finite element analysis to investigate stress distribution in the radius of toy poodles after screw removal. The examination focuses on the biomechanical implications of varied screw hole configurations using 1.5 and 2.0-mm locking compression plates (LCPs) with notched head T-Plates.

Aim: To provide a noninvasive approach to analyzing the immediate consequences of screw removal from the radius bone in toy poodles. Specifically, it explores the impact of varied plate designs and screw arrangements on stress distribution within the forelimb bones.

Methods: The study constructs a three-dimensional bone model of the toy poodle's forelimb based on computed tomography (CT) images. Simulations were designed to replicate jumping and landing from a 40 cm height, comparing stress distribution in the radius post-screw removal.

Results: The analysis reveals significant variations in stress distribution patterns between the two LCPs. The radius implanted with the 2.0-mm LCP displays a uniform stress distribution, contrasting with the 1.5-mm plates. Localized stress concentration is observed around the screw holes, while trabecular bone regions near the screw holes exhibit lower stress levels.

Conclusion: The study highlights the plate designs and screw configurations that affect bone stress in toy poodle forelimbs post-screw removal. The findings provide valuable insights for veterinarians, aiding informed decisions in veterinary orthopedic practices.

Keywords: Finite element analysis, Radius, Stress distribution, Toy poodle.

Introduction

Toy breed dogs, especially toy poodles, are admired for their small size and delightful personalities. Nevertheless, the attractive characteristics of these dogs frequently lead them to engage in activities that could potentially endanger their delicate skeletal structure. These dogs tend to jump and frequently participate in activities that strain their front legs, such as jumping from high places or falling out of a caregiver's hand (Bell *et al.,* 2022). This behavior heightens the risk of fractures and their fragile bone structure, especially in the distal radius and ulna, which are most commonly affected and fractured due to the force of impact (McCartney *et al.,* 2010; Yu *et al.,* 2010). Treating radius fractures in miniature poodle dogs presents a complex clinical situation that requires innovative approaches to ensure effective treatment and optimal post-operative outcomes. The small size, unique bone structure, and limited blood supply of toy poodles are essential features that make it challenging to treat fractures in these dogs (De Arburn Parent *et al.,* 2017; Aikawa *et al.,* 2018). These challenges require veterinarians to carefully analyze and employ specialized techniques to treat them, which could improve the probability of a successful recovery.

Locking compression plates (LCPs) have become a prominent choice in veterinary orthopedics for stabilizing fractures, offering exceptional stability and

***Corresponding Author:** Kenji Tani. Laboratory of Veterinary Surgery, Joint Faculty of Veterinary Medicine, Yamaguchi University, Japan. Email: *ktani@yamaguchi-u.ac.jp*

promoting healing. Previous studies (Haaland *et al.,* 2009; Gibert *et al.,* 2015; Kang *et al.,* 2016; Alwen *et al.,* 2018; Vezzoni *et al.,* 2021) have highlighted the benefits of LCPs, including the flexibility to choose screw types, preservation of critical blood supply, and optimal stability through the use of screws at multiple angles. Despite both 1.5 and 2.0-mm LCPs being employed for toy poodle radius fractures, there is a lack of evidence comparing their biomechanical properties. Several complications after the removal of screws have been reported, especially the occurrence of refracture in the radius (Haaland *et al.,* 2009; Vallefuoco *et al.,* 2016; De Arburn Parent *et al.,* 2017; Aikawa *et al.,* 2018). The choice of plate size is a critical decision influencing construction stability and healing. Moreover, the number and placement of screws significantly correlate with screw removal considerations during post-operative conditions, presenting a risk of refracture. Careful consideration regarding this situation is crucial during the decision-making process for screw removal, highlighting the need for ongoing research to refine fracture management guidelines and enhance long-term outcomes in veterinary orthopedic surgery.

The revolutionary impact of finite element analysis (FEA) in biomedical engineering is evident in its remarkable capabilities to address complex challenges. The methodology is pivotal in predicting biological responses to mechanical stimuli, facilitating efficient analysis of tissue deformation and stress distribution. This procedure has gained extensive traction in human medicine, primarily in elucidating fractures affecting the distal radius ulna (Johnson and Troy, 2017; Revel *et al.,* 2020; Yamazaki *et al.,* 2021; Pramudita *et al.,* 2022), its presence in veterinary orthopedics has been relatively limited. However, the evolving potential of FEA in veterinary orthopedics holds promise for addressing a range of complex challenges, offering insights into tissue deformation, stress distribution, and other biomechanical aspects. The interdisciplinary approach highlights FEA's versatility and potential contribution to human and veterinary medicine advancements.

To the best of our knowledge, there have been no studies that addressed the stress distribution on the toy poodle radius after the removal of screws using FEA. The primary objective is to investigate the biomechanical implications of post-operative screw removal in canine radius fractures. We hypothesize that the distribution of stress within the radius exhibits a substantial influence by both plate size and screw hole arrangement. The study employed a noninvasive FEA to investigate the stress distribution within the radius bones of canines as an alternative to experimental cadaveric investigations, addressing the constraints associated with such procedures.

Materials and Methods

Study subject and animal preparation

The experiment involved four-year-old toy poodles with a 3 kg body weight. The dogs were admitted to Yamaguchi University Animal Medical Centre as general patients with no orthopedic issues. The patient was required to fast for a minimum of 12 hours before the anesthetic procedure. An intravenous catheter was inserted into the dog's right cephalic vein using a 22-gauge needle (Terumo Company Ltd., Tokyo, Japan). Ringer's acetate solution (5 ml/kg/hours, Veen F, Fuso Pharmaceutical Industries Ltd., Osaka, Japan) was administered using an infusion pump (TOP-3300; TOP Corporation, Tokyo, Japan) throughout the procedure. Anesthesia induction started by administering propofol (Mylan®, Pfizer, Tokyo, Japan) intravenously at a dosage of 7 mg/kg. Following endotracheal intubation, anesthesia was maintained using an anesthetic machine (Dräger Fabius® Plus, Lübeck, Germany) that delivered isoflurane (Mylan®, Pfizer, Tokyo, Japan) through a rebreathing circuit. Continuous physiologic monitoring was accomplished utilizing a multiparameter monitor (BSM-6301, Life Scope, Nihon Kohden, Tokyo, Japan), which recorded electrocardiography, pulse oximetry, capnography, blood pressure, and core temperature readings. Regular anesthetic assessments were conducted at 5-minutes intervals, with findings documented by the anesthesiologist in the medical record.

Image acquisition and finite element model construction

The radius, ulna, humerus, and trabecular bone were isolated from 60 computed tomography (CT) scan images (Supria, Hitachi, Tokyo, Japan). A comprehensive three-dimensional model of the toy poodle forelimb was successfully constructed based on the segmentation of skeletal structures, as illustrated in Figure 1. Following the completion of segmentation on the model above, the subsequent steps include applying smoothing techniques to reduce noise and address gaps by fixing and meshing the model. To streamline the simulation, intentional avoidance of a fracture gap was implemented, and the plate was designed to stabilize a transverse fracture on the distal one-third of the radius bone.

The condition of the radius bone after screw removal was assessed by creating several holes based on the LCP 1.5 mm notched head T-plate (length, 36.25 mm; thickness, 1.0 mm; width of head, 9 mm; width of shaft, 4.25 mm; distance between center of shaft holes, 5.0 mm, six shaft holes, Code No. VP4007.06; DePuy Synthes Companies, Raynham, MA) and LCP 2.0 mm notched head T-plate (length, 54 mm; thickness, 1.33 mm; width of head, 12 mm; width of shaft, 5.0 mm; distance between center of shaft holes, 5.0 mm, seven shaft holes, Code No. VP4312.07; DePuy Synthes Companies, Raynham, MA). A hollow cylinder region was determined based on the screw hole diameters of 1.5 mm (Code No. VS106.011; DePuy Synthes

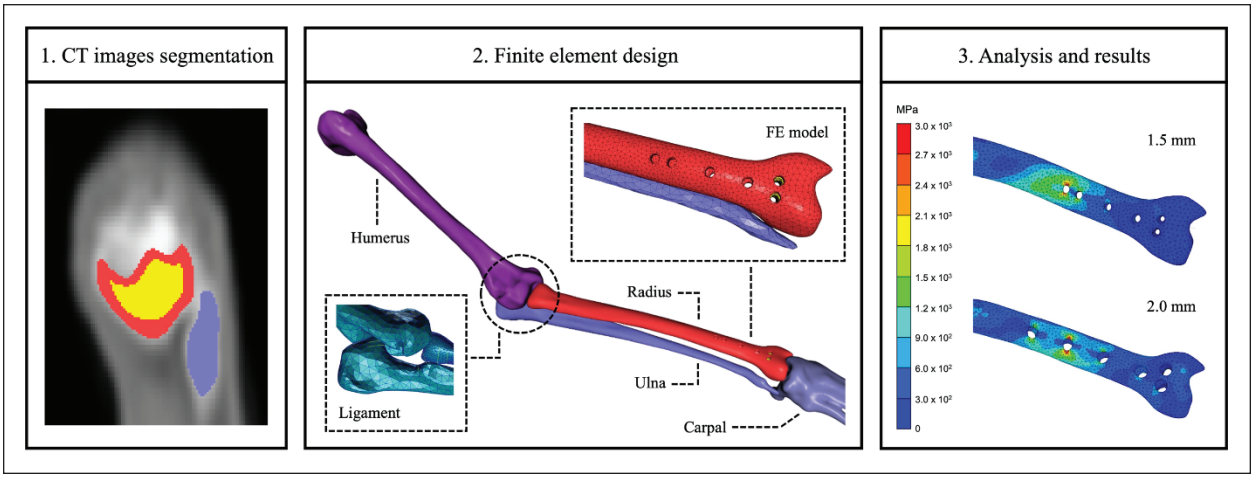

Fig. 1. Finite element design.

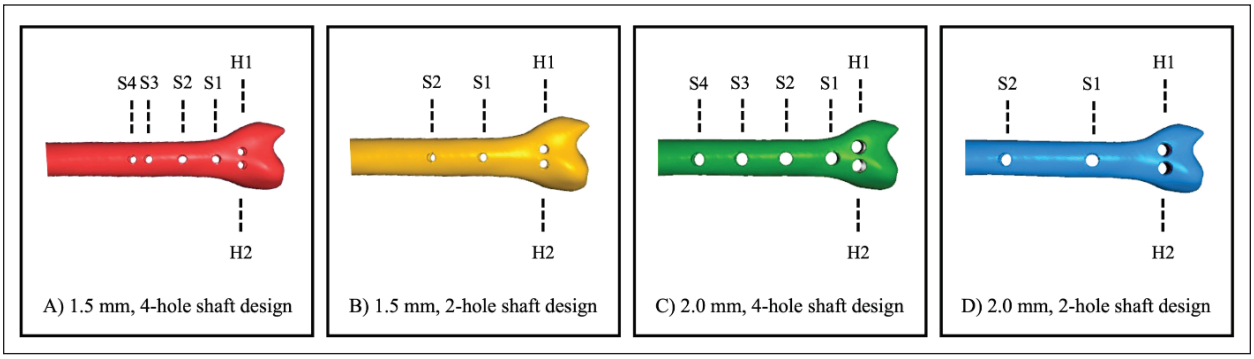

Fig. 2. Screw-hole arrangement on each plate. Head screw hole 1 (H1), head screw hole 2 (H2), shaft screw hole 1 (S1), shaft screw hole 2 (S2), shaft screw hole 3 (S3), and shaft screw hole 4 (S4).

Companies, Raynham, MA) and 2.0 mm (Code No. VS207.011; DePuy Synthes Companies, Raynham, MA) locking screw. Each cylindrical structure corresponds to the respective diameter screw hole sizes, illustrating 1.5 and 2.0 mm, respectively. The screw hole locations were created on the radius bone, and both sections of the head hole on each plate were inserted with screw holes. Simultaneously, the shaft holes for each plate were illustrated with two different arrangements: four holes and two holes (Fig. 2). These modifications not only replicate the screw removal process but also offer a comprehensive representation of post-surgery conditions. A normal radius without a screw hole was generated to facilitate a comparison to assess the bone's normal condition. The resulting model enhances understanding of how different screw configurations impact the structural integrity of the radius bone.

The experimental procedures described above were performed using Simpleware ScanIP v21 (Synopsis, Sunnyvale, CA). The finite element models utilized tetrahedral mesh elements with an average size of 0.2 mm. The element size for this component was selected through a rigorous analysis of convergence results, as it significantly influences the research findings. The carpal, ulna, and humerus shared identical elements and nodes for each plate model. Nevertheless, distinctions appeared when evaluating the positions of the screw holes (1.5 and 2.0 mm) in the radius and trabecular bones, especially in normal bone. Table 1 illustrates the different numbers of elements and nodes for all conditions.

Material properties and ligament creation

The humerus bone was represented as a homogeneous, isotropic, linearly elastic material (Synek *et al*., 2023). A high-resolution CT scan was conducted to differentiate between cortical and cancellous bone. Advanced image processing methods, notably thresholding and segmentation algorithms, were instrumental in accurately distinguishing cortical and cancellous bone. The subsequent verification process entailed aligning the segmented regions with different anatomical structures visible in the CT images, further substantiating this model's accuracy and biological

Table 1. Number of each element and nodes of each model.

Model	Element				Nodes			
	1.5 mm		2.0 mm		1.5 mm		2.0 mm	
	A	B	A	B	A	B	A	B
Humerus	41,147				7,106			
Ulna	15,160				3,828			
Carpal	6,452				2,050			
Trabecular	6,137	6,042	3,259	3,036	2,785	2,258	980	878
Radius	28,575	27,498	32,639	31,450	9,120	8,834	10,470	10,087

Table 2. Physical properties of bone material.

Element	Young modulus (MPa)	Poisson's ratio	Mass density (kg/mm^3)
Humerus	17,000	0.3	4.5×10^{-4}
Cortical	17,000	0.3	2.1×10^{-6}
Trabecular	350	0.3	7.0×10^{-7}

relevance. The data from earlier studies (Lai *et al.,* 2015; Laurent *et al.,* 2020; Hirashima *et al.,* 2021) were used to determine Young's modulus and Poisson's ratio of the humerus, cortical, and trabecular bone (Table 2). The humerus mass density was estimated by assuming that the forelimbs support 50% of the weight of a typical toy poodle, roughly 1.5 kg. The outcome was a humeral mass density of 4.5×10^{-4} kg/mm^3. In addition, the cortical and trabecular Young's modulus, Poisson's ratio, and bone mass density data were obtained from previous research (Table 2) (Helge, 1966).

Linear spring elements were implemented to model the biomechanical function of ligaments in connecting bones and stabilizing joints, as shown in Figure 1. These one-dimensional elastic springs produce a restoring force only when extended beyond their zero-load length, reflecting the physiological behavior of ligaments resisting tensile stress. The simplified representation allows the joint model to mimic ligament deformation under tensile loading and restrain hyperextension and dislocation. Specifically, the spring's zero-force length and stiffness properties were tuned to match the tension response of major ligamentous structures while keeping the articulating bones together within normal anisotropic limits.

Simulation condition

The boundary conditions were applied through the software MSC Patran v21 (Hexagon, Newport Beach, CA), followed by MSC Marc Mentat v21 (Hexagon, Newport Beach, CA) to conduct the analysis. The initial velocities of 2,800 mm/s were specifically applied to the humerus with a 0.0025 seconds timeframe partitioned into 800 increments, encompassing the critical event of fracture occurrence at ground contact. The above initial velocities represent drop heights of 40 cm, which display the most noticeable and appropriate disparities in the fracture mechanisms observed in toy-breed canines based on the preliminary research. The decision demonstrates to recreate the real-life situations experienced by these dogs during fall conditions, maximizing the efficiency of experimental resources and adopting an integrated approach that connects therapeutic significance with practical achievability. The carpals were fully constrained during the simulation to represent rigid contact with an unyielding ground plane. Equivalent landmark identifiers were systematically compiled from normal and screw-holed bone conditions, signifying the stress values. Subsequently, these data points were employed to facilitate a comprehensive comparative analysis. Von Mises stresses were determined within the radius under different loading circumstances to compare the impact of 1.5 and 2.0 mm LCP notched T-plate screw holes configurations on mechanical characteristics that lead to distal radius fractures.

Ethical approval

This study did not require ethical approval. The owners granted informed consent by completing and signing a consent form before the examination. The collected data were employed under anonymization protocols and general consent agreements.

Results

The analysis in Figure 3 compares von Mises stress distribution across one-third of the distal radius, considering various screw-hole locations. Regardless of screw hole configuration, LCP 2.0 mm shows a more uniform stress distribution than LCP 1.5 mm. Localized stress concentration around screw holes is consistent across all plate designs. Notably, the 4-hole shaft design exhibits the highest stress concentration at screw hole 4 for the 1.5 mm plate and screw hole 3 for

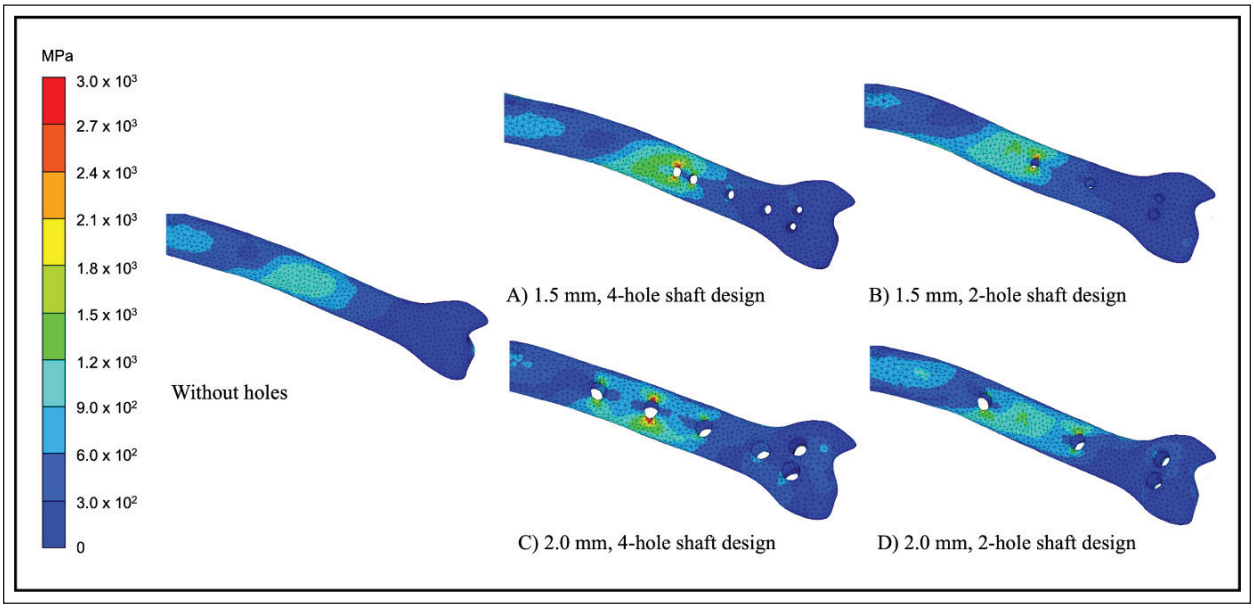

Fig. 3. Comparison of stress distribution with varying screw hole locations. The stress levels were illustrated using a color scale, where red signifies the most elevated stress zone.

the 2.0 mm plate. The 2-hole shaft design, however, displays distinct patterns, with the 1.5 mm design concentrating stress on screw hole 2, while the 2.0 mm design has consistent stress distribution between both screw holes. Importantly, stress concentration around trabecular screw holes is consistently lower than that around shaft screw holes across all plates. The stress values at each screw hole across all plates were described in the specific data provided below.

Four-hole screw shaft design

The stress values within the shaft screw holes of the normal bone showed the highest stress concentration at S3, registered at 1035.02 MPa (Fig. 4). The 1.5 mm plate resulted in elevated stress across all screw shaft locations, particularly at S4, reaching 1898.54 MPa. Similarly, the 2.0 mm plate exhibited a pronounced increase, notably at S3, where values surged from 1035.02 MPa in normal bone to 2586.39 MPa. Regarding the head screw, stress values around H1 and H2 in the normal bone were relatively lower at 86.9 and 123.72 MPa, respectively. However, the 1.5 mm plate led to a marked escalation, with stress levels significantly increasing to 372.24 and 332.8 MPa around H1 and H2, respectively. The 2.0 mm plate yielded elevated stress levels of 930.79 and 596.50 MPa around H1 and H2, respectively.

Two-hole screw shaft design

The stress values within the shaft screw holes of the normal bone demonstrated that the maximum stress concentration was observed at S2, reaching 1035.02 MPa (Fig. 5). The 1.5 mm plate screw hole increased stress at all configurations, especially at S2, where it reached 2264.78 MPa. Similar patterns were observed with the 2.0 mm plate, with stress at S2 rising from 1035.02 MPa in normal bone to 1848.36 MPa. Simultaneously when considering the head screw, stress levels around H1 and H2 were lower in normal bone (86.90 and 123.72 MPa, respectively). However, the 1.5 mm plate showed a substantial increase, reaching 384 MPa at H1 and 343.25 MPa at H2. The 2.0 mm plate design further heightened stress levels, with 760.04 MPa at H1 and 531.27 MPa at H2.

Discussions

Orthopedic veterinary practitioners frequently confront challenges and uncertainties during the post-operative phase, particularly when determining the optimal timing for the removal of screws from bone plates. FEA emerges as a sophisticated computational technique to navigate the complexities, enabling a thorough exploration of the mechanical interactions between bone and implant. The author's earlier experiment underscored concentrated stresses in the distal regions of the toy poodle's radius bones. The results align seamlessly with the present findings, reinforcing the consistent elevation of stress levels in the distal regions, as shown on the bones without holes (Fig. 3). The current study provides important findings on the mechanical dynamics of the radius bone, with a particular emphasis on the specific examination of stress distribution around the bone screws holes. The discovered findings remarkably advance the understanding of post-operative screw removal conditions in toy-breed dogs, offering fundamental insights into veterinary orthopedics.

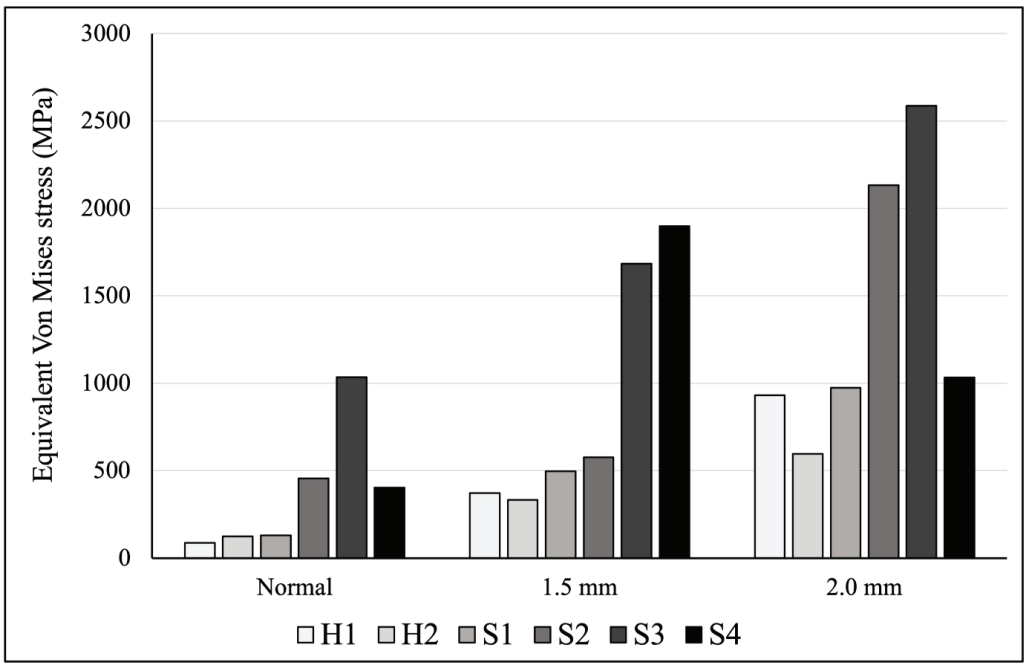

Fig. 4. Bar graph comparison of stress distribution on 4-hole screw shaft design.

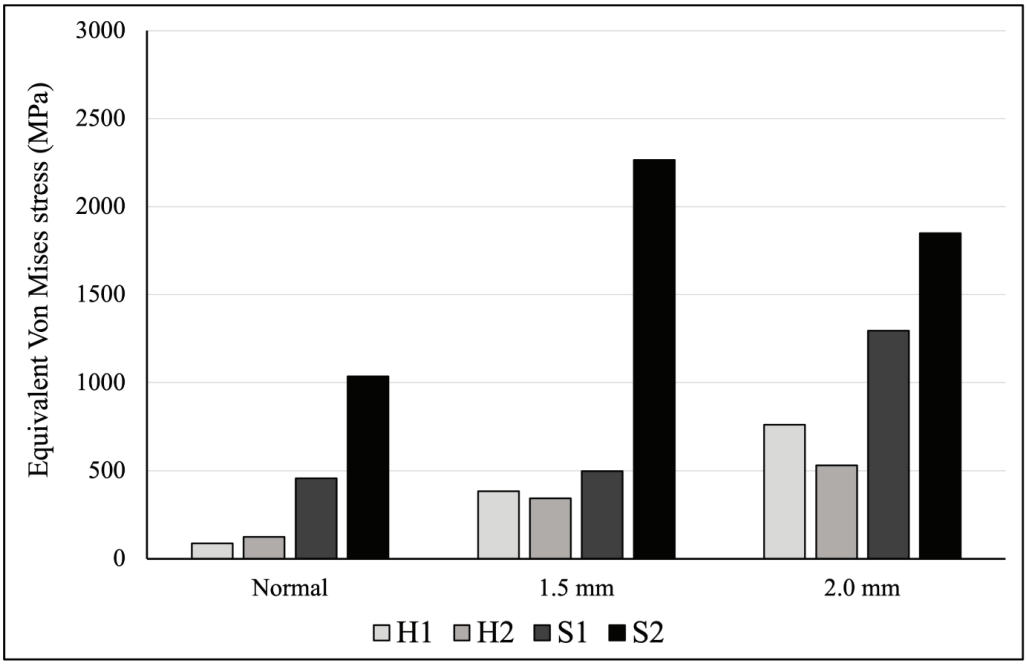

Fig. 5. Bar graph comparison of stress distribution on 2-hole screw shaft design.

Plates with longer lengths showed a more uniform stress distribution on the one-third distal radius. Interestingly, an increase in the number of screw holes in the plate was associated with heightened stress concentration around specific screw holes. The author's viewpoint regarding the present outcomes was that the plate length considerably influences stress distribution on the radius. The shorter plate has a limited area for stress distribution, leading to stress accumulation at the proximal region of the screw hole. Conversely, a longer plate enables a more uniform stress distribution. As shown by (El-Anwar and El-Zawahry, 2011; Erdem *et al.,* 2018), plate size and increased implant length would generate a uniform load distribution and improve

biomechanical performance. A recent study (Wang *et al.,* 2020; Valeri *et al*., 2024) similarly conveyed that various factors, including the working length of the plate, the presence of holes, the overall size of the plate, and the diameter and length of the screw, influence the mechanical environment around the bone. In addition, the study identified that the configuration of the shaft-hole screw, as shown by the four-hole shaft design, has a considerable effect on the stress level at a particular location. The rationale behind these results could be identified due to each screw hole insertion resulting in the removal of bone mass, diminishing the overall cross-sectional area (CSA) available for stress distribution. This condition leads to the remaining material around the screw holes being compelled to withstand an increased load, resulting in heightened stress levels. According to fundamental principles in the mechanics of materials, stress is defined as the internal force within a material divided by the CSA area over which the force acts. Following this, a diminished CSA raises stress levels when subjected to a specific applied load. Studies conducted by Nelson *et al.* (2000) and Zaki *et al.* (2015) found that the strength of long bones is mainly derived from the complex geometric details embedded in their cross-sectional structure. Bones with a larger CSA typically have greater bone mass and density. This characteristic facilitates the extensive distribution of bone tissue, enhancing its durability and capacity to endure bending or fractures. Further investigations have also indicated that bone mass and density are crucial in determining bone strength and impacting the possibility of fractures (Felder *et al.,* 2017; Pomeroy *et al.,* 2018; Jaworski *et al.,* 2019). These findings emphasize the importance of a comprehensive orthopedic strategy that considers both the mechanical stability offered by implants and their effect on the structural integrity of the bone.

Analysis of stress distribution across all plates revealed a concentrated accumulation of stress adjacent to the screw holes. These findings could be explained by the presence of screw holes, which create a structural irregularity resembling a defect in the bone. The presence of this discontinuity shape causes a disturbance in the uniform distribution of stress, leading to increased stress levels that are focused in the area surrounding the screw holes. The documented results agreed with Wolff's Law, emphasizing that bones adapt their structure in response to alterations in mechanical conditions to enhance their function (Dittmer and Firth, 2017). In other words, the bone undergoes a self-reinforcement process in regions with reduced bone mass, demonstrating its continual adaptation to stress distribution. Prior experimental research has supported our results (Rosson *et al.,* 1991), which showed that remaining screw holes have a substantial impact on bone weakening following plate removal, reducing the bone's absorbing capacity by approximately half. The weakening condition after the extraction of screws could initiate stress risers due to micro damage within the screw holes when receiving normal loads, compromising its structural integrity and heightening the risk of fractures (Velkes *et al.,* 1966; Zhou *et al.,* 2019; Yoo *et al.,* 2021). Our findings also resonate with (Largura *et al.,* 2014), which states that a greater magnitude of deformations developed at a close distance to the point of screw application. Similarly, (Bologna *et al.,* 2023) discovered elevated stress levels in areas surrounding the screw holes when evaluating the maximum stress and fatigue life of bone plates under in vivo loads.

The trabeculae region presented with the lowest amount of stress around the screw holes in comparison to the shaft screw holes on all plates. The author presumed that the variance in Young's modulus between cortical and trabecular bone might be associated with the different stress distributions. Cortical bone resists substantial elastic deformation under stress with its higher Young's modulus. In contrast, the trabecular bone's lower modulus allows for more significant elastic deformation and promotes a uniform stress distribution around screw holes. Existing evidence aligns with the findings (Currey, 2004a,b; Almer and Stock, 2007), indicating a positive correlation between the increase of Young's modulus in the cortical region and elevated stress along the bone. The observed phenomenon in the clinical condition can be attributed to the distinctive anatomical characteristics of trabecular bone. This region is designed with larger dimensions and a supportive network that efficiently distributes and absorbs stresses, surpassing cortical bone in the diaphyseal region. The porous structure of trabecular bone allows for superior stress distribution (Oftadeh *et al.,* 2015), making it well-suited to accommodate the forces associated with screw removal without creating localized stress points. Conversely, the cortical bone of the diaphyseal shaft, which has a significantly reduced porosity and less effective stress dissipation capabilities, resulted in the accumulation of stress, specifically adjacent to the screw hole. Remarkably, numerous FEA studies (Vijayalakshmi *et al.,* 2012; Barão *et al.,* 2013; Cicciù *et al.,* 2018; Kim *et al.,* 2023; Zhang *et al.,* 2023) have substantiated these clinical findings, consistently demonstrating that the trabecular region exhibits lower stress concentrations compared to the cortical region. The convergence of clinical observations and FEA outcomes underscores the robustness of trabecular bone's distinctive anatomical characteristics in providing superior stress distribution.

The current study has some limitations that should be acknowledged. Illustrating the complex interplay of anatomical features and physiological reactions in clinical scenarios, including the recreation of intricate biomechanics in the elbow and shoulder joints and simulating the complex muscle cushioning effects in FEA, poses a highly complex and challenging task. The authors intentionally excluded these complexities

to align with study objectives, acknowledging the necessary compromise between model intricacy and practical feasibility for achieving streamlined and relevant results.

Conclusion

Based on the data derived from this study, the longer plate design demonstrates superior and more uniformly distributed stress on the radius. Nevertheless, it is essential to note that there was a consistent observation of localized stress close to the screw holes. The findings underscore the importance of considering plate length and screw arrangement when evaluating stress distribution on the radius, especially in toy-breed dogs. This perceptive understanding substantially advances the comprehension of the dynamics associated with post-operative screw removal, offering invaluable insights for more informed clinical decision-making processes.

Acknowledgments

There are no acknowledgments to declare.

Conflict of interest

The authors declare that there is no conflict of interest.

Authors contributions

Conceptualization: D.A., F.J., and K.T. Investigation: D.A., M.S.P., H.I., K.I. Methodology: M.N., H.S., and K.T. Supervision: N.N., F.J., and K.T. Visualization: Y.N. and H.S. Writing—original draft: D.A. Writing—review and editing: D.A., F.J., and K.T.

Funding

This research received no specific grant.

Data availability

All data supporting the findings of this study are available in the manuscript.

References

Aikawa, T., Miyazaki, Y., Shimatsu, T., Iizuka, K. and Nishimura, M. 2018. Clinical outcomes and complications after open reduction and internal fixation utilizing conventional plates in 65 distal radial and ulnar fractures of miniature- and toy-breed dogs. Vet. Comp. Orthop. Traumatol. 31(3), 214–217.

Alwen, S.G.J., Kapatkin, A.S., Garcia, T.C., Milgram, J. and Stover, S.M. 2018. Open screw placement in a 1.5 mm LCP over a fracture gap decreases fatigue life. Front. Vet. Sci. 5(89), 1–7.

Almer, J.D. and Stock. S.R. 2007. Micromechanical response of mineral and collagen phases in bone. J. Struct. Biol. 157(2), 365–370.

Barão, V.A.R., Delben, J.A., Lima, J., Cabral, T. and Assunção, W.G. 2013. Comparison of different designs of implant-retained overdentures and fixed full-arch implant-supported prosthesis on stress distribution in edentulous mandible—a computed tomography-based three-dimensional finite element analysis. J. Biomech. 46(7), 1312–1320.

Bell, A.L., Rozanski, E.A. and Babyak, J. 2022. A multicenter retrospective comparison of trauma in toy breeds versus giant breeds: a veterinary committee on trauma registry study. J. Vet. Emerg. Crit. Care 32(1), 26–33.

Bologna, F.A., Audenino, A.L. and Terzini, M. 2023. An analytical and in silico strategy for estimating maximum stress and fatigue life of bone plates under in vivo loads: a rationale for regulatory testing. Front. Med. Eng. 1, 1241312.

Cicciù, M., Cervino, G., Milone, D. and Risitano, G. 2018. FEM investigation of the stress distribution over mandibular bone due to screwed overdenture positioned on dental implants. Materials 11(9), 1–17.

Currey, J. 2004a. Incompatible mechanical properties in compact bone. J. Theor. Biol. 231(4), 569–580.

Currey, J.D. 2004b. Tensile yield in compact bone is determined by strain, post-yield behaviour by mineral content. J. Biomech. 37(4), 549–556.

De Arburn Parent, R., Benamou, J., Gatineau, M., Clerfond, P. and Planté, J. 2017. Open reduction and cranial bone plate fixation of fractures involving the distal aspect of the radius and ulna in miniature and toy-breed dogs: 102 cases (2008–2015). J. Am. Vet. Med. Assoc. 250(12), 1419–1426.

Dittmer, K.E. and Firth, E.C. 2017. Mechanisms of bone response to injury. J. Vet. Diagn. Invest. 29(4), 385–395.

El-Anwar, M.I. and El-Zawahry, M.M. 2011. A three dimensional finite element study on dental implant design. J. Genet. Eng. Biotechnol. 9(1), 77–82.

Erdem, S., Gür, M. and Kaman, M.O. 2018. Static and dynamic analyses of fracture fixation bone-plate systems for different plate materials and dimensions. Biomed. Mater. Eng. 29(5), 611–628.

Felder, A.A., Phillips, C., Cornish, H., Cooke, M., Hutchinson, J.R. and Doube, M. 2017. Secondary osteons scale allometrically in mammalian humerus and femur. R. Soc. Open Sci. 4(11), 1–19.

Gibert, S., Ragetly, G.R., Boudrieau, R.J. 2015. Locking compression plate stabilization of 20 distal radial and ulnar fractures in toy and miniature breed dogs. Vet. and Comp. Orthop. Traumatol. 28(6), 441–447.

Haaland, P.J., Sjöström, L., Devor, M. and Haug, A. 2009. Appendicular fracture repair in dogs using the locking compression plate system: 47 cases. Vet. Comp. Orthop. Traumatol. 22(4), 309–315.

Helge, S. 1966. The breaking strength of normal and immobilized cortical bone from dogs, Acta Orthop. Scand, 37(2), 131–140.

Hirashima, T., Matsuura, Y., Suzuki, T., Akasaka, T., Kanazuka, A. and Ohtori, S. 2021. Long-term evaluation using finite element analysis of bone atrophy changes after locking plate fixation of

forearm diaphyseal fracture. J. Hand Surg. Glob. Online. 3(5), 240–244.
Jaworski, M., Wierzbicka, E., Pludowski, P. and Szalecki, M. 2019. Forearm bone density, cross-sectional size and muscle cross-sectional area in adolescents with diabetes mellitus type 1 assessed by peripheral quantitative computed tomography. J. Musculoskelet. Neuronal. Interact. 19(4), 435–447.
Johnson, J.E. and Troy, K.L. 2017. Validation of a new multiscale finite element analysis approach at the distal radius. Med. Eng. Phys. 44(1), 16–24.
Kang, B.J., Ryu, H.H., Park, S., Kim, Y., Kweon, O.K. and Hayashi, K. 2016. Clinical evaluation of a mini locking plate system for fracture repair of the radius and ulna in miniature breed dogs. Vet. Comp. Orthop. Traumatol. 29(6), 522–527.
Kim, J., Chun, B.J. and Kim, J.J. 2023. Quantitative load dependency analysis of local trabecular bone microstructure to understand the spatial characteristics in the synthetic proximal femur. Biology 12(2), 1–21.
Lai, Y.S., Chen, W.C., Huang, C.H., Cheng, C.K., Chan, K.K. and Chang, T.K. 2015. The effect of graft strength on knee laxity and graft in-situ forces after posterior cruciate ligament reconstruction. PLoS One 10(5), 1–11.
Largura, L.Z., Argenta, M.A., Sakima, M.T., Camargo, E.S., Guariza-Filho, O. and Tanaka, O.M. 2014. Bone stress and strain after use of a miniplate for molar protraction and uprighting: a 3-dimensional finite element analysis. Am. J. Orthod. Dentofacial. Orthop. 146(2), 198–206.
Laurent, C.P., Böhme, B., Verwaerde, J., Papeleux, L., Ponthot, J.P. and Balligand, M. 2020. Effect of orthopedic implants on canine long bone compression stiffness: a combined experimental and computational approach. Proc. Inst. Mech. Eng. H. 234(3), 255–264.
McCartney, W., Kiss, K. and Robertson, I. 2010. Treatment of distal radial/ulnar fractures in 17 toy breed dogs. Vet. Rec. 166(14), 430–432.
Nelson, D.A., Barondess, D.A., Hendrix, S.L. and Beck, T.J. 2000. Cross-sectional geometry, bone strength, and bone mass in the proximal femur in black and white postmenopausal women. J. Bone Miner. Res. 15(10), 1992–1997.
Oftadeh, R., Perez-Viloria, M., Villa-Camacho, J.C., Vaziri, A. and Nazarian, A. 2015. Biomechanics and mechanobiology of trabecular bone: a review. J. Biomech. Eng. 137(1), 0108021–01080215.
Pomeroy, E., Macintosh, A., Wells, J.C.K., Cole, T.J. and Stock, J.T. 2018. Relationship between body mass, lean mass, fat mass, and limb bone cross-sectional geometry: implications for estimating body mass and physique from the skeleton. Am. J. Phys. Anthropol. 166(1), 56–69.
Pramudita, J.A., Hiroki, W., Yoda, T. and Tanabe, Y. 2022. Variations in strain distribution at distal radius under different loading conditions. Life 12(5), 1–12.
Revel, M., Bermond, F., Mitton, D. and Follet, H. 2020. Specimen-specific finite element prediction of surface strain at the distal radius in a fall configuration. Comput. Methods Biomech. Biomed. Engin. 23(1), S257–S259.
Rosson, J., Egan, J., Shearer, J. and Monro, P. 1991. Bone weakness after the removal of plates and screws cortical atrophy or screw holes? J. Bone Joint Surg. 73(2), 283–286.
Synek, A., Ortner, L. and Pahr, D.H. 2023. Accuracy of osseointegrated screw-bone construct stiffness and peri-implant loading predicted by homogenized FE models relative to micro-FE models. J. Mech. Behav. Biomed. Mater. 140, 105740.
Valeri, C., Aloisio, A., Quinzi, V., Stefano, G. and Marzo, G. 2024. Characterizing orthodontic mini-screws in the hard palate of pigs: an experimental and finite-element study. Heliyon 10(3), e24952.
Vallefuoco, R., Le Pommellet, H., Savin, A., Decambron, A., Manassero, M., Viateau, V., Gauthier, O. and Fayolle, P. 2016. Complications of appendicular fracture repair in cats and small dogs using locking compression plates. Vet. and Comp. Orthop. Traumatol. 29(1), 46–52.
Velkes, S., Nerubay, J., Lokiec, F. 1966. Stress fracture of the proximal femur after screw removal. Arch. Orthop. Trauma Surg. 115(1), 61–62.
Vezzoni, L., Abrescia, P. and Vezzoni, A. 2021. Internal radioulnar fixation for treatment of nonunion of proximal radius and ulna fractures in a toy breed dog. Vet. and Comp. Orthop. Traumatol. 4(1), e24–e31.
Vijayalakshmi, P., Veereshi, A., Jayade, V.P., Dinesh, M. and Kumar, M. 2012. Finite element analysis of stress and strain distribution in the bone around the implants used for orthodontic anchorage. J. Indian Orthod. Soc. 46(4), 175–182.
Wang, J., Zhang, X., Li, S., Yin, B., Liu, G., Cheng, X. amd, Zhang, Y. 2020. Plating system design determines mechanical environment in long bone mid-shaft fractures: a finite element analysis. J. Investig. Surg. 33(8), 699–708.
Yamazaki, T., Matsuura, Y., Nimura, A., Horiuchi, S., Suzuki, T. and Ohtori, S. 2021. Prediction of stress distribution applied to the triangular fibrocartilage complex: a finite element analysis. J. Hand Surg. Glob. Online 3(2), 94–98.
Yoo, J., Ma, X., Lee, J. and Hwang, J. 2021. Research update on stress riser fractures. Indian J. Orthop. 55(3), 560–570.
Yu, J., DeCamp, C.E. and Rooks, R. 2010. Improving surgical reduction in radial fractures using a

"dowel" pinning technique in miniature and toy breed dogs. Vet. and Comp. Orthop. Traumatol. 24(1), 45–49.

Zaki, M.E., Azab, A.A., Yousef, W., Wassal, E.Y. and El-Bassyouni, H.T. 2015. Cross-sectional analysis of long bones in a sample of ancient Egyptians. Egyptian J. Radiol. Nucl. Med. 46(3), 675–681.

Zhang, J., Li, H., Zhou, Y., Chen, S. and Rong, Q. 2023. An analysis of trabecular bone structure based on principal stress trajectory. Bioengineering 10(10), 1–12.

Zhou, S., Jung, S. and Hwang, J. 2019. Mechanical analysis of femoral stress-riser fractures. Clin. Biomech. 63(1), 10–15.